Standoff Boundary in Ultraviolet Non-Line-of-Sight Covert Communication

Tao Shan, *Graduate Student Member, IEEE*, Nan He, *Graduate Student Member, IEEE*, and Julian Cheng, *Fellow, IEEE*.

Abstract—Ultraviolet (UV) communication is widely known for its local confidentiality due to rapid signal attenuation over distance. However, the inherent low background interference in UV communication environments can make signal transmission more easily detectable by an eavesdropper. In this study, we introduce covert communication metrics based on overall photon counting and peak power to assess analytically the covert performance of UV non-line-of-sight (NLOS) communications on photon counting channels. By integrating the covert metrics with the UV omni-directional NLOS channel model, we demonstrate standoff boundaries for the first time. Our simulation results confirm the effectiveness of UV NLOS covert communication and offer vital insights into the design and operational strategies of UV NLOS covert communication systems.

Index Terms—Covert communication, optical non-line-of-sight transmission, ultraviolet communications

I. INTRODUCTION

Optical wireless communication (OWC) capitalizes on the substantial license-free transmission bandwidth while avoiding electromagnetic radiation [1]. Among many types of OWC, ultraviolet (UV) communication offers a unique capability for non-line-of-sight (NLOS) transmissions, enabled by the intense atmospheric scattering of the UV-C band coupled with exceptionally low background radiation near the Earth's surface. Thus, UV NLOS communication can serve as a vital alternative in scenarios where radio-frequency (RF) signals are impractical and conventional free-space-optical line-of-sight links are unreliable [2]–[4].

Besides its capability for NLOS transmitting, UV communication is also recognized for its strong regional confidentiality, primarily due to two distinctive features of the UV-C spectral band. First, UV-C light is invisible to the human eye and standard optical or electronic sensors, producing no obvious emission that would alert an eavesdropper to an active link. To detect UV signals, an eavesdropper must not only know that UV is in use but also possess specialized photodetectors and filtering systems [5]. This uncommon spectral usage forms the first layer of confidentiality for UV communication. Second, UV-C undergoes much stronger attenuation near the Earth's surface than other communication bands because of the significant atmospheric scattering and absorption of UV-C signals [3], [6]. The attenuation induced by the atmosphere rapidly dissipates UV-C beams, thereby restricting their effective signal to a highly localized area. This strong attenuation

Tao Shan, Nan He, and Julian Cheng are with the School of Engineering, the University of British Columbia, Kelowna, BC, Canada, (e-mail: tao.shan@ubc.ca; nan.he@ubc.ca; julian.cheng@ubc.ca).

provides a second layer of confidentiality by limiting how far the communication can propagate. However, if an eavesdropper positions advantageously and uses equipment specifically designed for UV-C detection, the inherent low background interference in such environments may make transmissions easier to detect than expected. Standoff distance was first introduced to quantify the low probability detection in UV communication [7]. Nevertheless, this standoff distance was only derived from a point-wise channel gain. Further, the standoff distance estimate was obtained numerically without any physical insights. Therefore, a more comprehensive and insightful analysis of the secure communication boundary of NLOS UV communication is needed [2].

The transmission characteristics of the UV signal, particularly their attenuation properties, are fundamental to understanding standoff distance. These characteristics have been extensively investigated in the existing channel modeling literature. These models often rely on Monte Carlo simulations [8]–[10] or analytical approximations [11]–[13] to capture the strong atmospheric attenuation and scattering of UV-C. In particular, Monte Carlo based multi-scattering channel models are commonly used to simulate long-range NLOS transmission attenuation [14], while single-scattering analytical approximations are typically more suitable for short-range scenarios [11], [15]. Additionally, an omni-directional channel model has been introduced for two-dimensional broadcast communications in NLOS settings [16], and the impact of various weather conditions on UV transmission coverage was theoretically studied [17].

Studies on secure NLOS UV communication predominantly focus on physical-layer approaches; however, the literature in this area remains limited. Among various physical layer-based security schemes, three principal methodologies have emerged as mainstream approaches for ensuring secure communications: physical layer security (PLS), spread spectrum techniques, and covert communication [18]. PLS enhances secrecy by reducing the signal-to-interference-plus-noise ratio at the eavesdropper's end, thereby preventing the decoding of secure data, with the secrecy rate serving as the theoretical metric. Specifically, the secrecy rate based on PLS in NLOS UV channels was analyzed under two communication protocols: non-jamming and cooperative jamming [19].

Unlike PLS, spread spectrum techniques and covert communication are designed to blend communication signals with noise, making detection by eavesdroppers difficult. Spread spectrum is a practical method for this purpose, but it lacks comprehensive analytical models and well-defined metrics

to assess its theoretical security performance [18]. On the other hand, covert communication seeks to minimize the detectability of signals by increasing the lower bound of the eavesdropper's error probability when attempting any hypothesis test on the presence of a transmission [20]–[22]. The key metric in covert communication is the relative entropy between the probability distributions of channel observations when the transmission is present versus absent. In current UV communication research, a spread spectrum-based scheme for UV communication has been proposed and validated through simulations and experiments [23]. This scheme's covertness was assessed under binary hypothesis testing and the Kolmogorov-Smirnov test.

In this study, we focus on employing covert communication-based metrics to analyze the security performance and standoff boundaries in UV NLOS communications. The standoff boundary is defined such that an eavesdropper located beyond this boundary has difficulty accurately determining the presence of a transmission. Meanwhile, the standoff boundary is a two-dimensional extension of the standoff distance, where the farthest point on the boundary from the transmitter represents the standoff distance, typically on the transmitter's orientation. Considering that the most critical metric in covert communication is the relative entropy between the distributions of channel observations with and without transmission, we derive the relative entropy for various channel observation strategies in both pure-loss photon counting channels[1] and bandwidth-limited photon counting channels. Our derivation yields a lower bound for the eavesdropper's error probability in photon counting channels. This analytical expression can provide a comprehensive characterization of the security performance of UV communication. Furthermore, by integrating the proposed metrics with the updated UV omni-directional channel model, we establish the standoff boundaries and coverage area for UV omni-directional communications. The patterns of standoff boundaries and communication coverage areas are also analyzed with respect to the elevation angles of the transmitter and receiver, the eavesdropper's error probability, and the amounts of covertly transmitted information bits. Our numerical results indicate that UV NLOS communication can maintain a standoff distance of $2000\,\mathrm{m}$, while supporting the NLOS covert transmission of $100\,\mathrm{kbits}$ of information over hundreds of meters.

II. OMNI-DIRECTIONAL NLOS UV COVERT COMMUNICATION

Figure 1 depicts the typical scenario of omni-directional NLOS UV covert communication. Alice broadcasts signals under NLOS conditions to communicate stealthily with all friendly users, such as Bob, within a specific area. Simultaneously, adversarial eavesdroppers, such as Willie, monitor the area to ascertain the presence of Alice. In this study, we assume the presence of Alice is equivalent to the presence of Alice's active transmission. This study considers only one-way communication from Alice to Bob, without a duplex

[1]The term 'pure loss photon counting channel' refers to a channel model that only considers channel path loss, excluding bandwidth limitations induced by multipath effects due to scattering.
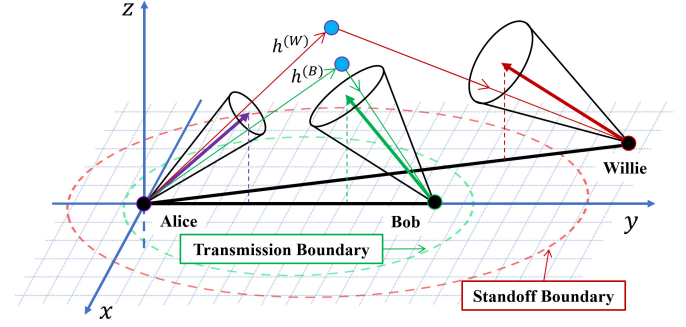

Fig. 1. Schematic diagram of UV NLOS covert transmission.

link or return transmission from Bob that could introduce an additional transmitter [24], [25]. Transmission boundary refers to the maximum communication range within which Alice ensures that Bob can demodulate the broadcast signal with an error rate below a predetermined threshold. Standoff Boundary denotes the minimum range at which Alice can guarantee that the probability of Willie detecting the broadcast signal remains below a specified threshold. In Figure 1, $h^{(B)}$ and $h^{(W)}$ are the impulse response of Alice-to-Bob channel and Alice-to-Willie channel, respectively. The proposed UV NLOS communication scenario does not incorporate cooperative jamming, because we focus on the intrinsic covert capability of UV signals under natural background noise.

The UV NLOS communication system typically operates within a photon domain characterized by low signal power, minimal noise levels, and adherence to Poisson statistics [26]. As a result, signal transmission predominantly employs unipolar pulse modulation, while signal reception relies on photon counting mechanisms. The unipolar pulse modulation for each time slot can be described by a slot indicator sequence, $\{x[a]\}$, where $x[a] = 0$ signifies the absence of a pulse emission, and $x[a] = 1$ indicates its presence in the respective time slot. Accordingly, the transmitted optical signal can be expressed as $x(t) = \sum_a x[a]P_{\mathrm{on}}p(t - aT_s)$, where P_{on} is the maximum transmitted optical power and $p(t)$ represents the unit square pulse spanning the interval $[0, T_s]$. Thus, the arrived optical power $I(t)$ can be derived through the convolution of the transmitted signal $x(t)$ with the channel impulse response (CIR) $h(t)$, specifically given by

$$\begin{aligned} I(t) &= h(t) \otimes x(t) + \gamma_n \\ &= P_{\mathrm{on}}h_g \sum_a \left(x[a]p(t - aT_s) \otimes \overline{h}(t)\right) + \gamma_n, \end{aligned} \quad (1)$$

where $\otimes$ denotes the convolution operator and γ_n is the sum of the equivalent non-time-varying background radiation power and the equivalent dark current input power; $h_g \triangleq \int h(t)\mathrm{d}t$ defines the channel gain and $\overline{h}(t)$ is the normalized CIR, normalized by h_g.

Given the substantial path loss associated with scattering-based NLOS channels, the arriving optical power $I(t)$ in (1) manifests at the receiver as a rate of photon arrivals. Consequently, the output at the photon-counting receiver can be described by a non-homogeneous Poisson counting process

$\{Y_s(t), t \geq 0\}$ with intensity function $\lambda(t) = \frac{\eta_r}{h\nu}I(t)$, where η_r denotes the product of the filter transmittance and the quantum efficiency of the photodetector; h and ν are Plank constant and the frequency of the UV signal, respectively. For any time interval $[t_1, t_2]$ where $0 \leq t_1 \leq t_2$, the probability that the photon count increments by k is given by

$$\Pr\{Y_s(t_2) - Y_s(t_1) = k\} = \frac{\left(\int_{t_1}^{t_2} \lambda(t)\mathrm{d}t\right)^k}{k!} e^{-\int_{t_1}^{t_2} \lambda(t)\mathrm{d}t}. \tag{2}$$

In the absence of Alice and her signal transmission, the slot indicator sequence $\{x[a]\}$ remains constantly zero. Thus, the output of the photon counting receiver degenerates into a homogeneous Poisson counting process $\{Y_0(t), t \geq 0\}$ consisting solely of noise contributions γ_n, i.e.,

$$\Pr\{Y_0(t_2) - Y_0(t_1) = k\} = \frac{\left(\frac{\eta_r \gamma_n}{h\nu}(t_2 - t_1)\right)^k}{k!} e^{-\frac{\eta_r \gamma_n}{h\nu}(t_2 - t_1)}. \tag{3}$$

III. COVERT COMMUNICATION METRIC

Covert communication fundamentally requires that Willie, based on his channel observations, cannot conclusively determine Alice's presence. Specifically, the signals received by Willie should exhibit similar characteristics regardless of whether Alice's transmission is active or not. When Alice's transmission is active, the probabilistic characteristics of Willie's received signals are fully described by the Poisson counting process $\{Y_s(t), t \geq 0\}$ in (2). Conversely, in the absence of Alice's transmission, the corresponding probabilistic characteristics conform entirely to the process $\{Y_0(t), t \geq 0\}$ in (3).

We assume that Willie performs a statistical hypothesis test on the received signals, with the null hypothesis H_0 positing Alice's absence and the alternative hypothesis H_1 asserting her presence. The prior probabilities for each hypothesis being true are considered equal. Thus, the probability of discrimination error, $P_e^{(W)}$ can be lower bounded as [21]

$$P_e^{(W)} \geq \frac{1}{2} - \sqrt{\frac{1}{8}\mathcal{D}\left(\mathbb{P}_0 \| \mathbb{P}_1\right)} \triangleq P_{e,L}^{(W)}, \tag{4}$$

where $\mathbb{P}_0$ and $\mathbb{P}_1$ are the respective probability distributions of observations when hypotheses H_0 and H_1 are true; $\mathcal{D}\left(\mathbb{P}_0 \| \mathbb{P}_1\right)$ is the relative entropy (also known as Kullback-Leibler divergence) between $\mathbb{P}_0$ and $\mathbb{P}_1$, which quantifies the discrepancy between the two probability distributions. Accordingly, the stealth capabilities of covert communication can be effectively analyzed using $\mathcal{D}\left(\mathbb{P}_0 \| \mathbb{P}_1\right)$. When the discrepancy between $\mathbb{P}_0$ and $\mathbb{P}_1$ is sufficiently minimal, the probability of discrimination error in Willie's hypothesis testing approaches the level associated with making a random guess without any observational data.

Although the relative entropy is a convenient metric for assessing the stealth capabilities of covert communication, its calculation depends on the specific distribution of Willie's observations of the channel, which is governed by the Poisson counting processes outlined in (2) and (3). In this section, we present several forms of channel observation distribution

and subsequently analyze the stealth capabilities of photon counting based communication in detail.

A. Pure-Loss Photon Counting Channel

In this paper, we define the pure-loss channel as one that exclusively accounts for channel path loss, intentionally omitting the effects of bandwidth limitations typically induced by the multipath effects in scattering-based channels. In this scenario, the CIR $h^{(W)}(t)$ in (1) can be modeled by a scaled Dirac delta function, i.e., $h^{(W)}(t) = h_g^{(W)}\delta(t)$, where $h_g^{(W)}$ denotes the channel gain of Alice-to-Willie channel. Thus, when Alice transmits signals according to a finite-length slot indicator sequence $\{x[a]\}$ within the time interval $[0, T]$, the intensity function of the Poisson counting process $\{Y_s(t), 0 \leq t \leq T\}$ can be expressed as

$$\lambda^{(W)}(t) = \lambda_s^{(W)} \sum_a x[a]p(t - aT_s) + \lambda_n, \quad 0 \leq t \leq T, \tag{5}$$

where $\lambda_s^{(W)} = \frac{P_{on}\eta_r h_g^{(W)}}{h\nu}$ represents the average signal photon counts per second; $\lambda_n = \frac{\gamma_n \eta_r}{h\nu}$ accounts for the average noise counts per second. Without loss of generality, we assume that the ratio $\frac{T}{T_s}$ is an integer. In the pure-loss channel, the unit square wave pulse function $p(t)$ serves as the fundamental component for describing received optical intensity.

1) Observation Based on Total Photon Counting: Willie observes the channel by counting all photons during the window that coincides with Alice's transmission interval $[0, T]$. He subsequently uses the aggregate photon count for hypothesis testing. We can have the following result on the upper bound of the relative entropy.

Theorem 1. *When Willie observes the pure-loss channel based on total photon counting within $[0, T]$, the relative entropy between the probability distributions of the total photon count, corresponding to whether Alice is transmitting or not, can be upper bounded by*

$$\mathcal{D}\left(\mathbb{P}_0^{\mathrm{I}} \| \mathbb{P}_1^{\mathrm{I}}\right) \leq \frac{Td^2}{2} \frac{\left(\lambda_s^{(W)}\right)^2}{\lambda_n}, \tag{6}$$

where $\mathbb{P}_1^{\mathrm{I}}$ and $\mathbb{P}_0^{\mathrm{I}}$ denote the distribution of total counts when Alice is transmitting or not, respectively; $d = \frac{T_s}{T}\sum_a x[a]$ represents the equivalent duty cycle of the emission signal within the overall transmission interval $[0, T]$. The equality sign is achieved when $\lambda_s^{(W)}$ tends to zero.

Proof. Since the channel characteristics follow the Poisson counting process, the total photon count W^{I} follows the Poisson distribution. Denote by $\mathbb{P}_1^{\mathrm{I}}$ the distribution of W^{I} when Alice transmits and by $\mathbb{P}_0^{\mathrm{I}}$ the distribution when she does not transmit. Therefore, the probability mass function (PMF) of $\mathbb{P}_1^{\mathrm{I}}$ is given by

$$p_{1,W^{\mathrm{I}}}\left(w^{\mathrm{I}}\right) = \frac{(\Lambda_n + \Lambda_s)^{w^{\mathrm{I}}} e^{-(\Lambda_n + \Lambda_s)}}{w^{\mathrm{I}}!}, \tag{7}$$

where $\Lambda_s = Td\lambda_s^{(W)}$ and $\Lambda_n = T\lambda_n$ are the mean signal counts and mean noise counts within the interval $[0, T]$, respectively. Meanwhile, the PMF of $\mathbb{P}_0^{\mathrm{I}}$ is given by

$$p_{0,W^{\mathrm{I}}}\left(w^{\mathrm{I}}\right) = \frac{\Lambda_n^{w^{\mathrm{I}}} e^{-\Lambda_n}}{w^{\mathrm{I}}!}. \tag{8}$$

Notably, due to the characteristics of Poisson distribution, having Λ_s less than Λ_n is a necessary condition for the feasibility of covert communication, particularly when the time interval T is substantially larger than T_s. However, this condition alone does not suffice to guarantee the indistinguishability of the signal from the noise.

The relative entropy between $\mathbb{P}_0^{\mathrm{I}}$ and $\mathbb{P}_1^{\mathrm{I}}$ can be calculated as follows:

$$\begin{aligned} \mathcal{D}\left(\mathbb{P}_0^{\mathrm{I}}\|\mathbb{P}_1^{\mathrm{I}}\right) &= \sum_{w^{\mathrm{I}}=0}^{\infty} p_{0,W^{\mathrm{I}}}\left(w^{\mathrm{I}}\right) \ln \frac{p_{0,W^{\mathrm{I}}}\left(w^{\mathrm{I}}\right)}{p_{1,W^{\mathrm{I}}}\left(w^{\mathrm{I}}\right)} \\ &= \Lambda_s - \Lambda_n \ln \left(1 + \frac{\Lambda_s}{\Lambda_n}\right) \\ &= \frac{\Lambda_s^2}{2\Lambda_n} - \Lambda_n \Delta_1 \\ &\leq \frac{\Lambda_s^2}{2\Lambda_n} \\ &= \frac{Td^2 \left(\lambda_s^{(W)}\right)^2}{2 \lambda_n}. \end{aligned} \tag{9}$$

Here, we apply the Mercator series to expend $\ln\left(1 + \frac{\Lambda_s}{\Lambda_n}\right)$. The remainder term, denoted by $\Delta_1 = \frac{\Lambda_s^3}{3\Lambda_n^3} - \frac{\Lambda_s^4}{4\Lambda_n^4} + \cdots$, is non-negative and captures higher-order corrections. $\qquad\square$

Theorem 1 quantifies the covert communication performance in UV NLOS environments. Considering our primary focus on assessing the security standoff range, as shown in Fig. 1, Willie's position is generally assumed to be further from Alice than Bob's position. Consequently, additional path loss reduces $\lambda_s^{(W)}$, thereby diminishing $\mathcal{D}\left(\mathbb{P}_0^{\mathrm{I}}\|\mathbb{P}_1^{\mathrm{I}}\right)$.

From the perspective of transmitting a slot indicator sequence $\{x[a]\}$, a decrease in the number of optical slot pulses results in a lower average duty cycle of emission, which subsequently decreases the relative entropy $\mathcal{D}\left(\mathbb{P}_0^{\mathrm{I}}\|\mathbb{P}_1^{\mathrm{I}}\right)$. Essentially, total photon counting serves as a method of energy accumulation detection, analogous to cumulative power detection in additive white Gaussian noise channels. Higher energy transmissions increase the probability of detection by eavesdroppers. Therefore, modulation schemes with higher energy efficiency are better suited for covert communication, exemplified by the inherent superiority of pulse position modulation (PPM) over on-off keying (OOK) in terms of covert characteristics. In this study, we specifically employ a PPM modulation of order Q, where the equivalent duty cycle d is equal to $\frac{1}{Q}$. Thus, eq. (9) becomes

$$\mathcal{D}\left(\mathbb{P}_0^{\mathrm{I}}\|\mathbb{P}_1^{\mathrm{I}}\right) \leq \frac{T}{2Q^2} \frac{\left(\lambda_s^{(W)}\right)^2}{\lambda_n} = \frac{BT_s}{2Q\log_2 Q} \frac{\left(\lambda_s^{(W)}\right)^2}{\lambda_n}, \tag{10}$$

where B denotes the total number of covertly transmitted information bits. Both Theorem 1 and (10) suggest that

covert transmission becomes infeasible if Alice continuously transmits an infinite number of bits while Willie extends his observation window indefinitely, even with the additional path loss differentiation between the intended and eavesdropping channels. Therefore, designing a short burst of information bits is recommended to achieve covert transmission.

2) Observation Based on Bernoulli Process: When Willie divides the observation time interval [0, T] into numerous counting windows of sufficiently small duration τ, the Poisson counting process can be approximated by a Bernoulli process. This process can be denoted by $\mathbf{W}^{\mathrm{II}} = \left\{W_j^{\mathrm{II}}\right\}_{j=1}^{J_2}$, where $W_j^{\mathrm{II}} \in \{0, 1\}$ and $J_2 = \frac{T}{\tau}$.

Let $\mathbb{P}_{0,W_j^{\mathrm{II}}}$ denote the distribution of W_j^{II} when Alice does not transmit, and $\mathbb{P}_{1,W_j^{\mathrm{II}}}$ denote the distribution when she transmits. Thus, the PMF of $\mathbb{P}_{0,W_j^{\mathrm{II}}}$ is expressed as

$$p_{0,W_j^{\mathrm{II}}}\left(w_j^{\mathrm{II}}\right) = (1 - \lambda_n\tau)^{1-w_j^{\mathrm{II}}} \left(\lambda_n\tau\right)^{w_j^{\mathrm{II}}}. \tag{11}$$

In the scenario where Alice transmits Q-PPM signals, the distribution of W_j^{II} is a mixed Bernoulli distribution. Specifically, W_j^{II} follows a Bernoulli distribution, taking the parameter $\lambda_n\tau$ with a probability $1 - \frac{1}{Q}$, and $\lambda_n\tau + \lambda_s^{(W)}\tau$ with a probability $\frac{1}{Q}$. Consequently, the PMF of $\mathbb{P}_{1,W_j^{\mathrm{II}}}$ is given by

$$\begin{aligned} p_{1,W_j^{\mathrm{II}}}\left(w_j^{\mathrm{II}}\right) &= \left(1 - \lambda_n\tau - \frac{\lambda_s^{(W)}\tau}{Q}\right)^{1-w_j^{\mathrm{II}}} \\ &\times \left(\lambda_n\tau + \frac{\lambda_s^{(W)}\tau}{Q}\right)^{w_j^{\mathrm{II}}}. \end{aligned} \tag{12}$$

The relative entropy between $\mathbb{P}_{0,W_j^{\mathrm{II}}}$ and $\mathbb{P}_{1,W_j^{\mathrm{II}}}$ is calculated by

$$\begin{aligned} &\mathcal{D}\left(\mathbb{P}_{0,W_j^{\mathrm{II}}}\|\mathbb{P}_{1,W_j^{\mathrm{II}}}\right) \\ &= (\lambda_n\tau - 1)\left(\frac{-\frac{\lambda_s^{(W)}\tau}{Q}}{1 - \lambda_n\tau} + \Delta_2\right) - \lambda_n\tau \ln\left(1 + \frac{\lambda_s^{(W)}}{Q\lambda_n}\right) \end{aligned} \tag{13}$$

with the remainder $\Delta_2 = -\frac{1}{2}\left(\frac{-\frac{\lambda_s^{(W)}\tau}{Q}}{1-\lambda_n\tau}\right)^2 + \cdots$.

Then, we define $\mathbb{P}_0^{\mathrm{II}}$ and $\mathbb{P}_1^{\mathrm{II}}$ as the distributions of the observation sequence $\mathbf{W}^{\mathrm{II}}$ under non-transmission and transmission conditions, respectively. Using (13), we can obtain the relative entropy between $\mathbb{P}_0^{\mathrm{II}}$ and $\mathbb{P}_1^{\mathrm{II}}$ as follows:

$$\begin{aligned} \mathcal{D}\left(\mathbb{P}_0^{\mathrm{II}}\|\mathbb{P}_1^{\mathrm{II}}\right) &= \lim_{\tau \to 0} \frac{T}{\tau} \mathcal{D}(\mathbb{P}_{0,W_j^{\mathrm{II}}}\|\mathbb{P}_{1,W_j^{\mathrm{II}}}) \\ &= \frac{T}{2Q^2} \frac{\left(\lambda_s^{(W)}\right)^2}{\lambda_n} - T\lambda_n\Delta_1 \\ &\equiv \mathcal{D}(\mathbb{P}_0^{\mathrm{I}}\|\mathbb{P}_1^{\mathrm{I}}), \end{aligned} \tag{14}$$

where Δ_1 has been defined in (9). The equality $\mathcal{D}(\mathbb{P}_0^{\mathrm{II}}\|\mathbb{P}_1^{\mathrm{II}}) = \mathcal{D}(\mathbb{P}_0^{\mathrm{I}}\|\mathbb{P}_1^{\mathrm{I}})$ at the end of (14) indicates that the observational approaches based on the total photon count channel and approximate Bernoulli channel yield equivalent discriminability between signal and noise from a statistical perspective.

3) Observation Based on Synchronized Segmented Photon Counting: When Willie happens to know the start instants and duration T_s of each slot of Alice's transmitted pulse signals, and subsequently counts photons in each slot, the output of the channel observation is a sequence of mutually independent Poisson-distributed elements, denoted by $\mathbf{W}^{\mathrm{III}} = \left\{ W_j^{\mathrm{III}} \right\}_{j=1}^{J_3}$, where $W_j^{\mathrm{III}} \in \mathbb{N}_0$ and $J_3 = \frac{T}{T_s}$ represents the number of slots.

Let $\mathbb{P}_{0,W_j^{\mathrm{III}}}$ denote the distribution of W_j^{III} when Alice does not transmit, and $\mathbb{P}_{1,W_j^{\mathrm{III}}}$ denote the distribution when she transmits. Thus, the PMF of $\mathbb{P}_{0,W_j^{\mathrm{III}}}$ is written as

$$p_{0,W_j^{\mathrm{III}}}\left(w_j^{\mathrm{III}}\right) = \frac{(\lambda_n T_s)^{w_j^{\mathrm{III}}} e^{-\lambda_n T_s}}{w_j^{\mathrm{III}}!}. \tag{15}$$

In the scenario where Alice transmits Q-PPM signals, the distribution of W_j^{III} can be expressed by a mixed Poisson distribution. Specifically, W_j^{III} follows a Poisson distribution, taking the parameter $\lambda_n T_s$ with a probability $1 - \frac{1}{Q}$, and $(\lambda_n + \lambda_s^{(W)})T_s$ with a probability $\frac{1}{Q}$. Then, the PMF of $\mathbb{P}_{1,W_j^{\mathrm{III}}}$ is given by

$$p_{1,W_j^{\mathrm{III}}}\left(w_j^{\mathrm{III}}\right) = \frac{Q-1}{Q} \cdot \frac{(\lambda_n T_s)^{w_j^{\mathrm{III}}} e^{-\lambda_n T_s}}{w_j^{\mathrm{III}}!} + \frac{1}{Q} \frac{\left((\lambda_n + \lambda_s^{(W)}) T_s \right)^{w_j^{\mathrm{III}}} e^{-(\lambda_n + \lambda_s^{(W)}) T_s}}{w_j^{\mathrm{III}}!}. \tag{16}$$

The relative entropy between $\mathbb{P}_{0,W_j^{\mathrm{III}}}$ and $\mathbb{P}_{1,W_j^{\mathrm{III}}}$ can be calculated by

$$\begin{aligned} &\mathcal{D}\left(\mathbb{P}_{0,W_j^{\mathrm{III}}} \| \mathbb{P}_{1,W_j^{\mathrm{III}}} \right) \\ &= \sum_{w_j^{\mathrm{III}}=0}^{\infty} p_{0,W_j^{\mathrm{III}}}\left(w_j^{\mathrm{III}}\right) \ln \left[\frac{p_{0,W_j^{\mathrm{III}}}\left(w_j^{\mathrm{III}}\right)}{p_{1,W_j^{\mathrm{III}}}\left(w_j^{\mathrm{III}}\right)} \right] \\ &= -\sum_{w_j^{\mathrm{III}}=0}^{\infty} p_{0,W_j^{\mathrm{III}}}\left(w_j^{\mathrm{III}}\right) \\ &\quad \times \ln \left[1 - \frac{1}{Q} + \frac{e^{-\lambda_s^{(W)} T_s}}{Q} \left(1 + \frac{\lambda_s^{(W)}}{\lambda_n} \right)^{w_j^{\mathrm{III}}} \right]. \end{aligned} \tag{17}$$

We define $\mathcal{D}\left(\mathbb{P}_{0,W_j^{\mathrm{III}}} \| \mathbb{P}_{1,W_j^{\mathrm{III}}} \right) \triangleq f\left(\frac{1}{Q} \right)$. Given that Theorem 1 requires $\frac{1}{Q}$ to be sufficiently small to reduce the discriminability between signal and noise, we employ a Taylor series expansion of the function $f\left(\frac{1}{Q} \right)$ around $\frac{1}{Q} = 0$, expressed as:

$$f\left(\frac{1}{Q} \right) = f(0) + \frac{f'(0)}{1!} \frac{1}{Q} + \frac{f''(0)}{2!} \frac{1}{Q^2} + \frac{f'''(0)}{3!} \frac{1}{Q^3} + \cdots, \tag{18}$$

where $f(0) = f'(0) = 0$ and $\frac{f''(0)}{2Q^2}$ can be calculated as

$$\frac{f''(0)}{2Q^2} = \frac{1}{2Q^2} \frac{\left(\lambda_s^{(W)} \right)^2 T_s}{\lambda_n} + \frac{1}{2Q^2} \sum_{i=2}^{\infty} \frac{1}{i!} \left(\frac{\left(\lambda_s^{(W)} \right)^2 T_s}{\lambda_n} \right)^i \tag{19}$$

with a detailed derivation provided in the Appendix A. Since $\frac{\left(\lambda_s^{(W)} \right)^2 T_s}{\lambda_n} \leq 1$ happens based on the requirement from Theorem 1, $f\left(\frac{1}{Q} \right)$ behaves similarly to the first term of (19). Moreover, we define $\mathbb{P}_0^{\mathrm{III}}$ and $\mathbb{P}_1^{\mathrm{III}}$ as the distributions of the observation sequence $\mathbf{W}^{\mathrm{III}}$ under non-transmission and transmission conditions, respectively. Using (19), we can obtain the relative entropy between $\mathbb{P}_0^{\mathrm{III}}$ and $\mathbb{P}_1^{\mathrm{III}}$ as follows:

$$\mathcal{D}\left(\mathbb{P}_0^{\mathrm{III}} \| \mathbb{P}_1^{\mathrm{III}} \right) = \frac{T}{T_s} \mathcal{D}(\mathbb{P}_{0,W_j^{\mathrm{III}}} \| \mathbb{P}_{1,W_j^{\mathrm{III}}}) \approx \frac{T}{2Q^2} \frac{\left(\lambda_s^{(W)} \right)^2}{\lambda_n}, \tag{20}$$

where the approximate result is obtained by neglecting the higher-order terms in (19) and is consistent with the upper bound presented in (10).

Following the detailed discussion on the relative entropy across three observational approaches, as presented in (10), (14), and (20), we ascertain that the upper bound presented in Theorem 1 effectively quantifies the discriminability between signal and noise in a pure-loss photon counting channel. Additionally, it characterizes the stealth properties of pulse-based signals in covert communication.

B. Bandwidth-Limited Photon Counting Channel

Compared to the pure-loss photon counting channel, bandwidth-limited channels account for the temporal dispersion of signal pulses caused by multipath effects in long-distance scattering-based channels, where the CIR cannot be modeled as a scaled Dirac delta function. Thus, the fundamental component describing the intensity of the reception Poisson process is no longer represented by the square wave pulse $p(t)$, but instead by a time-extended slot pulse function $r^{(W)}(t)$. The function $r^{(W)}(t)$ is derived by convolving the unit square wave pulse with the CIR. Therefore, within the interval $\{0 \leq t \leq T\}$, the intensity function of the Poisson counting process is given by

$$\begin{aligned} \lambda_{\mathrm{L}}^{(W)}(t) &= \lambda_s^{(W)} \sum_a x[a] p(t - aT_s) \otimes \overline{h}^{(W)}(t) + \lambda_n \\ &= \lambda_s^{(W)} \sum_a x[a] r^{(W)}(t - aT_s) + \lambda_n, \end{aligned} \tag{21}$$

where $\overline{h}^{(W)}(t)$ denotes the normalized CIR of Alice-to-Willie channel, normalized with respect to Willie's channel gain $h_g^{(W)}$.

We assume the slot pulse function $r^{(W)}(t)$ spans Q_d slots. Given that in covert communications, Q_d is typically much smaller than Q. We can neglect the effects of slot pulse spreading on the extension of the transmission interval $[0, T]$. Therefore, the covert metric based on total counting observations in bandwidth-limited channels is fundamentally consistent with that in pure-loss channels, confirming the broad applicability of Theorem 1 across different channel conditions.

For considering the observational method based on the Bernoulli process, when Alice transmits, the PMF of Bernoulli

This article has been accepted for publication in IEEE Transactions on Wireless Communications. This is the author's version which has not been fully edited and content may change prior to final publication. Citation information: DOI 10.1109/TWC.2025.3564322

6

process element $W_{\mathrm{L},j}^{\mathrm{II}}$ can be modified from (12) as

$$
\begin{aligned}
& p_{1,W_{\mathrm{L},j}^{\mathrm{II}}}\left(w_{\mathrm{L},j}^{\mathrm{II}}\right) \\
& = \left(1 - \lambda_n\tau - \frac{\lambda_s^{(W)}\tau}{T_sQ}\sum_{i=1}^{\left\lfloor\frac{Q_dT_s}{\tau}\right\rfloor}r^{(W)}(i\tau)\tau\right)^{1-w_{\mathrm{L},j}^{\mathrm{II}}} \\
& \quad\times\left(\lambda_n\tau + \frac{\lambda_s^{(W)}\tau}{T_sQ}\sum_{i=1}^{\left\lfloor\frac{Q_dT_s}{\tau}\right\rfloor}r^{(W)}(i\tau)\tau\right)^{w_{\mathrm{L},j}^{\mathrm{II}}} \\
& \approx \left(1 - \lambda_n\tau - \frac{\lambda_s^{(W)}\tau}{Q}\right)^{1-w_{\mathrm{L},j}^{\mathrm{II}}}\left(\lambda_n\tau + \frac{\lambda_s^{(W)}\tau}{Q}\right)^{w_{\mathrm{L},j}^{\mathrm{II}}}.
\end{aligned}
$$
(22)

The final approximation holds because the chosen value of τ is small, such that the summation operation approximates an integral operation, and the integral of $r^{(W)}(t)$ over its domain equals T_s. From the result presented in (12) and (22), the distribution of the Bernoulli process based observations in the bandwidth-limited is identical to that in the pure-loss channel. The covert communication metrics in both channels are identical.

When Willie observes the bandwidth-limited channel during Alice's transmissions using synchronized segmented photon counting, the Poisson distribution $\mathbb{P}_{1,W_{\mathrm{L},j}^{\mathrm{III}}}$ governing the segmented counting elements $W_{\mathrm{L},j}^{\mathrm{III}}$ is different from the distribution in pure-loss channels. The modified PMF of $\mathbb{P}_{1,W_{\mathrm{L},j}^{\mathrm{III}}}$ can be derived from (16) as

$$
\begin{aligned}
p_{1,W_{\mathrm{L},j}^{\mathrm{III}}}\left(w_{\mathrm{L},j}^{\mathrm{III}}\right) = {} & \frac{Q-Q_d}{Q}\frac{(\lambda_nT_s)^{w_{\mathrm{L},j}^{\mathrm{III}}}e^{-\lambda_nT_s}}{w_{\mathrm{L},j}^{\mathrm{III}}!} \\
& + \sum_{i=1}^{Q_d}\frac{1}{Q}\frac{\left(\lambda_nT_s+\Lambda_{s,i}^{(W)}\right)^{w_{\mathrm{L},j}^{\mathrm{III}}}e^{-\left(\lambda_nT_s+\Lambda_{s,i}^{(W)}\right)}}{w_{\mathrm{L},j}^{\mathrm{III}}!},
\end{aligned}
$$
(23)

where $\Lambda_{s,i}^{(W)} = \lambda_s^{(W)}\int_{\varepsilon+(i-1)T_s}^{\varepsilon+iT_s}r^{(W)}(t)\mathrm{d}t$ denotes the signal cumulative rate in Poisson distribution, with ε representing the segmented counting-start instant. When Alice's transmission does not exist, the observational element $W_{\mathrm{L},j}^{\mathrm{III}}$ follows the distribution $\mathbb{P}_{0,W_j^{\mathrm{III}}}$ with the PMF as specified in (15).

The relative entropy between $\mathbb{P}_{0,W_j^{\mathrm{III}}}$ and $\mathbb{P}_{1,W_{\mathrm{L},j}^{\mathrm{III}}}$ can be calculated by

$$
\begin{aligned}
& \mathcal{D}\left(\mathbb{P}_{0,W_j^{\mathrm{III}}}\|\mathbb{P}_{1,W_{\mathrm{L},j}^{\mathrm{III}}}\right) \\
& = \sum_{w_{\mathrm{L},j}^{\mathrm{III}}=0}^{\infty}p_{0,W_j^{\mathrm{III}}}\left(w_{\mathrm{L},j}^{\mathrm{III}}\right)\ln\left[\frac{p_{0,W_j^{\mathrm{III}}}\left(w_{\mathrm{L},j}^{\mathrm{III}}\right)}{p_{1,W_{\mathrm{L},j}^{\mathrm{III}}}\left(w_{\mathrm{L},j}^{\mathrm{III}}\right)}\right] \\
& = -\sum_{w_{\mathrm{L},j}^{\mathrm{III}}=0}^{\infty}p_{0,W_j^{\mathrm{III}}}\left(w_{\mathrm{L},j}^{\mathrm{III}}\right) \\
& \quad\times\ln\left[1-\frac{Q_d}{Q}+\frac{1}{Q}\sum_{i=1}^{Q_d}e^{-\Lambda_{s,i}^{(W)}}\left(1+\frac{\Lambda_{s,i}^{(W)}}{\lambda_nT_s}\right)^{w_{\mathrm{L},j}^{\mathrm{III}}}\right].
\end{aligned}
$$
(24)

We define $\mathcal{D}\left(\mathbb{P}_{0,W_j^{\mathrm{III}}}\|\mathbb{P}_{1,W_{\mathrm{L},j}^{\mathrm{III}}}\right) \triangleq f_{\mathrm{L}}\left(\frac{1}{Q}\right)$. Based on the Taylor series expansion in (18), we can obtain $f_{\mathrm{L}}(0) = f_{\mathrm{L}}'(0) = 0$ and

$$
\frac{f_{\mathrm{L}}''(0)}{2Q^2} \approx \frac{1}{2Q^2}\sum_{m=1}^{Q_d}\sum_{n=1}^{Q_d}\frac{\Lambda_{s,m}^{(W)}\Lambda_{s,n}^{(W)}}{\lambda_nT_s} = \frac{1}{2Q^2}\frac{\left(\lambda_s^{(W)}\right)^2T_s}{\lambda_n},
$$
(25)

which is equal to the dominant part in (19). Details of the derivation are provided in the Appendix B. Based on (9), (19), and (25), the relative entropy of the segmented photon count sequences in both pure loss channels and bandwidth-limited channels performs similar to the upper bound introduced in Theorem 1.

C. Peak Power Constraint

In the previous parts of this section, we have focused on the overall covert communication performance of UV NLOS communications throughout the complete transmission interval. However, considering that the UV communication environment typically features low signal strength and low noise, compliance with Theorem 1 for the overall covert communication configuration does not guarantee covert communication at the individual slot duration scale. This absence of stealth becomes particularly evident when employing high transmission powers, especially in conjunction with paralyzable photon detectors such as Photomultiplier Tubes (PMTs) used by Willie. For instance, when Alice transmits using UV high-energy pulsed lasers, Willie can receive a photoelectric pulse signal characterized by sharp rising and falling edges, but with a width significantly broader than the single photon pulse. Such signals are practically non-existent in a natural environment and could potentially be identified using threshold detection techniques on the rising edge.

Considering that excessively high peak power can impair the stealth capabilities of UV NLOS communications, we continue to apply relative entropy to quantify the distinguishability between photon count distributions with and without emission signals at the scale of a single slot. When bandwidth limitations are ignored, photon counts in a signal-transmission slot follow the Poisson distribution $\mathbb{P}_{1,p,T_s}$ with the parameter $(\lambda_s^{(W)}+\lambda_n)T_s$. Conversely, the noise counts within one slot adhere to the Poisson distribution identical to $\mathbb{P}_{0,W_j^{\mathrm{III}}}$ as defined in (15). Thus, the relative entropy between $\mathbb{P}_{0,W_j^{\mathrm{III}}}$ and $\mathbb{P}_{1,p,T_s}$ is calculated as

$$
\mathcal{D}\left(\mathbb{P}_{0,W_j^{\mathrm{III}}}\|\mathbb{P}_{1,p,T_s}\right) = \lambda_s^{(W)}T_s + \lambda_nT_s\ln\left(\frac{\lambda_n}{\lambda_s^{(W)}+\lambda_n}\right).
$$
(26)

Building upon the relationship between the probability of discrimination error and the relative entropy in (4), we can obtain a peak power based lower bound for the probability of discrimination error in scenarios where Willie's observations rely on signal-level detection. The peak power based lower bound aims to preserve the covert nature of UV transmission by preventing the emergence of noticeable slot pulses.

IV. COVERT TRANSMISSION PERFORMANCE WITH BOB

In the Alice-to-Bob covert channel, the primary concerns are both the accuracy and the distance over which Bob can receive the information bits covertly transmitted from Alice. The intensity function of the Poisson counting process received by Bob can be obtained by

$$
\begin{aligned}
\lambda_{\mathrm{L}}^{(B)}(t) &= \frac{P_{\mathrm{on}}\eta_r h_g^{(B)}}{h\nu} \sum_a x[a] p(t - aT_s) \otimes \overline{h}^{(B)}(t) + \lambda_n \\
&= \frac{P_{\mathrm{on}}\eta_r h_g^{(B)}}{h\nu} \sum_a x[a] r^{(B)}(t - aT_s) + \lambda_n,
\end{aligned}
\tag{27}
$$

where $\overline{h}^{(B)}(t)$ denotes the normalized impulse response of Alice-to-Bob channel, normalized with respect to Bob's channel gain $h_g^{(B)}$. Notably, given that the receiver can be located anywhere within the two-dimensional simulation area, the geometry of the scattering-based link varies substantially across different receiving locations. As a result, some positions experience substantial time dispersion in their CIR $\overline{h}^{(B)}(t)$, which introduces inter-symbol interference (ISI), whereas others exhibit negligible time dispersion. Furthermore, to maintain a practical transmission rate, we employ a microsecond-scale pulse-position modulation slot duration, which is short enough to amplify ISI in locations where the CIR exhibits strong time dispersion. Consequently, we incorporate ISI effects at all receiver positions when evaluating their communication performance. We assume that in short-range NLOS communication, the slot pulse will only diffuse into the two adjacent slots [27]. Additionally, given that covert communications require high-order PPM, the effect of the slot pulse's temporal dispersion within one PPM symbol on the demodulation of another PPM symbol is considered negligible.

We employ the bit error rate (BER), denoted by $P_e^{(B)}$, to characterize the communication performance of the Alice-to-Bob channel. Since the BER approximates half of the symbol-error rate in high-order PPM systems [28], the BER can be written as

$$
P_e^{(B)} \approx \frac{1}{2}\left(1 - P_{c,s}^{(B)}\right)
\tag{28}
$$

where $P_{c,s}^{(B)}$ denotes the probability of correct soft-decision decoding for a Q-ary PPM symbol. Specifically, the decoder selects the slot with the highest photon count as the signal slot. If multiple slots share the highest count, the decoder randomly picks one among them. Consequently, $P_{c,s}^{(B)}$ can be decomposed into three components:

$$
P_{c,s}^{(B)} = p_0 + p_1 + p_2,
\tag{29}
$$

where p_0 denotes the probability that all PPM slots contain zero photons and yet decoding is correct, which can be written as

$$
p_0 = \frac{1}{Q}\left(e^{-\lambda_n T_s}\right)^{Q-3} e^{-(\Lambda_0 + \Lambda_1 + \Lambda_{-1})}.
\tag{30}
$$

Importantly, Λ_0, Λ_1, and Λ_{-1} are the Poisson cumulative rates of pulse slot and two adjacent interference slots, respectively. Since the photon counting receiver is analogous

to an Integrate-and-Dump receiver, the cumulative rates can be calculated by $\Lambda_a = \lambda_n T_s + \lambda_s^{(B)} \int_{\varepsilon_s + aT_s}^{\varepsilon_s + (a+1)T_s} r^{(B)}(t)\mathrm{d}t$, where ε_s denotes the counting-start instant, which is related to the signal delay experienced by the receiver on a specific position and can be determined by the maximum correlation synchronization [29]. Moreover, p_1 denotes the probability that the signal slot strictly exceeds all other slots in photon count, which can be calculated by

$$
\begin{aligned}
p_1 &= \sum_{b_0=1}^{\infty} \frac{(\Lambda_0)^{b_0} e^{-\Lambda_0}}{b_0!} \left(\sum_{b_{-1}=0}^{b_0-1} \frac{(\Lambda_{-1})^{b_{-1}} e^{-\Lambda_{-1}}}{b_{-1}!}\right) \\
&\times \left(\sum_{b_1=0}^{b_0-1} \frac{(\Lambda_1)^{b_1} e^{-\Lambda_1}}{b_1!}\right) \left(\sum_{n=0}^{b_0-1} \frac{(-\lambda_n T_s)^n e^{-\lambda_n T_s}}{n!}\right)^{Q-3}.
\end{aligned}
\tag{31}
$$

In (29), p_2 denotes the probability that more than one slot has the same largest count, but the correct slot is chosen. Because computing p_2 can be complex in high-order PPM symbol decoding, we introduce the lower bound by omitting p_2 and including only p_0 and p_1. As a result, the corresponding upper bound on the BER follows naturally from the inequality above, i.e.,

$$
\begin{aligned}
P_e^{(B)} &\leq P_{e,\mathrm{U}}^{(B)} \\
&= \frac{1}{2}\left(1 - p_0 - p_1\right) \\
&= \frac{1}{2} - \frac{1}{2Q}\left(e^{-\lambda_n T_s}\right)^{Q-3} e^{-(\Lambda_0 + \Lambda_1 + \Lambda_{-1})} \\
&\quad - \frac{1}{2}\sum_{b_0=1}^{\infty} \frac{(\Lambda_0)^{b_0} e^{-\Lambda_0}}{b_0!} \left(\sum_{b_{-1}=0}^{b_0-1} \frac{(\Lambda_{-1})^{b_{-1}} e^{-\Lambda_{-1}}}{b_{-1}!}\right) \\
&\quad \times \left(\sum_{b_1=0}^{b_0-1} \frac{(\Lambda_1)^{b_1} e^{-\Lambda_1}}{b_1!}\right) \left(\sum_{n=0}^{b_0-1} \frac{(-\lambda_n T_s)^n e^{-\lambda_n T_s}}{n!}\right)^{Q-3}.
\end{aligned}
\tag{32}
$$

V. SIMULATION RESULTS AND ANALYSIS

In this section, we employ a Monte Carlo based omni-directional transmission model to simulate NLOS channel gain patterns within a specified area [16], [30]. While this model effectively maps the general attenuation characteristics across diverse locations, it lacks the capability to provide the detailed CIRs necessary for precise calculations of Bob's BER. To address this limitation, we enhance our approach by integrating a CIR simulation module from a point-to-point channel model [10], thereby enriching our simulations with the detailed temporal dynamics required for BER analysis. Detailed descriptions of the upgraded models are available in the Appendix C.

In the omni-directional communication scenario shown in Fig. 1, the elevation angle and divergence angle of Alice are denoted by α_T and β_T, respectively. We assume that the quantum efficiency and filter transmittance of Willie's receiver are identical to those of Bob's, with both receivers oriented

This article has been accepted for publication in IEEE Transactions on Wireless Communications. This is the author's version which has not been fully edited and content may change prior to final publication. Citation information: DOI 10.1109/TWC.2025.3564322

8

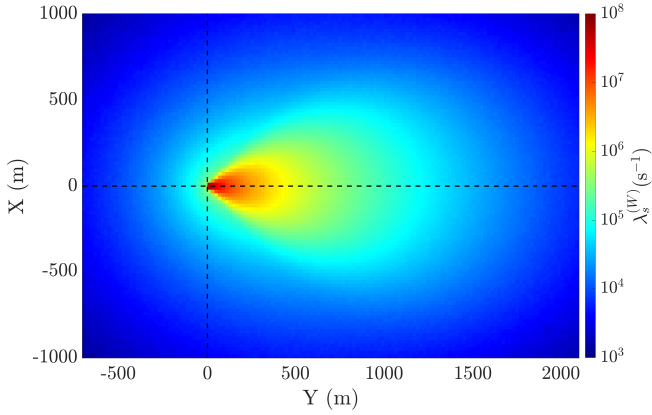| Parameters	Value
P_{ON}	2 W
T_s	2 µs
B	50 kbits
$[\eta_f, \eta_p]$	[0.4, 0.3]
λ_n	$1 \times 10^5 \,\mathrm{s}^{-1}$
$[\alpha_T, \beta_T]$	$[45°, 15°]$
$[\alpha_{\mathrm{B},R}, \beta_{\mathrm{B},R}]$	$[45°, 60°]$
$[\alpha_{\mathrm{W},R}, \beta_{\mathrm{W},R}]$	$[45°, 60°]$
c	$2.997\,046 \times 10^8 \,\mathrm{m\,s}^{-1}$
h	$6.626\,070 \times 10^{-34} \,\mathrm{J \cdot s}$
λ	265 nm
ν	$1.13 \times 10^{15} \,\mathrm{Hz}$
η_r	0.12

Fig. 2. Spatial distribution of Willie's signal photon rates across the region in the omni-direction NLOS transmission ($\alpha_{\mathrm{W},R} = 90°$).
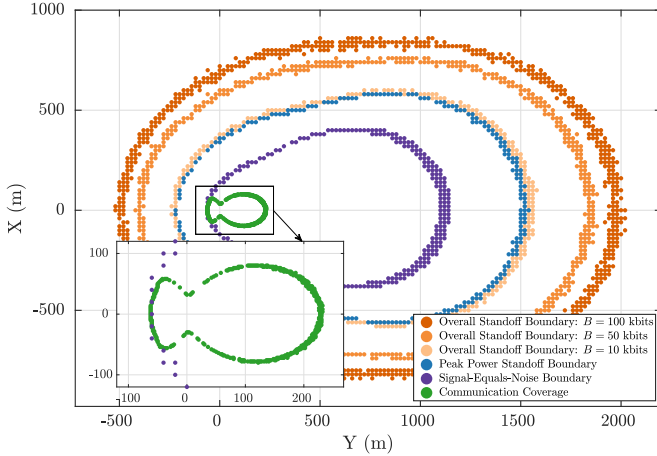

Fig. 3. Boundary patterns of UV NLOS transmission for different amounts of covert information.

towards Alice's location. Bob's elevation angle and field-of-view (FOV) are represented by $\alpha_{\mathrm{B},R}$ and $\beta_{\mathrm{B},R}$, respectively, while Willie's are denoted by $\alpha_{\mathrm{W},R}$ and $\beta_{\mathrm{W},R}$. The simulation parameters in the omni-directional UV transmission are shown in Table I.

Figure 2 illustrates the simulated spatial distribution of Willie's signal photon rates, $\lambda_s^{(W)}$, across the region under omni-directional NLOS transmission conditions. This simulation assumes Willie has no knowledge of Alice's position and sets his receiver's elevation angle at $90°$, yet Willie's detection interval aligns with Alice's transmission interval. The results in Fig. 2 demonstrate that regardless of the direction, Willie's signal photon rates decrease rapidly as the distance between Willie and Alice increases. Additionally, the corresponding standoff boundaries of NLOS covert transmission are shown in Fig. 3. The standoff boundary is defined where Willie's lower bound of the probability of discrimination error is 47%, closely approximating the 50% error rate of random guessing. The chosen value of 47% illustrates that even with channel measurements, the error rate remains close to random guessing, indicating that those measurements do not offer sufficient information to reliably determine whether a transmission is occurring. Specifically, the overall standoff boundaries are simulated using the covert metric based on overall photon counting in Theorem 1, while the peak power standoff boundaries use the covert metric based on peak power constraints in (26). The communication coverage is defined where Bob's upper bound of the BER is less than 3.5×10^{-3}.

Figure 3 shows a significant disparity exists between the communication and standoff boundaries. This is because of the contrasting energy requirements between Bob's signal reception mode and Willie's channel monitoring mode. Bob's mode necessitates energy accumulation within each small symbol interval for effective decoding, whereas Willie's mode capitalizes on the total received energy throughout the entire time interval for a single binary decision. This distinction highlights the inherent challenges of achieving covert communication from a system perspective. Besides, transmitting more information bits necessitates increased photon emission, thereby requiring an expanded standoff boundary to introduce a more significant path loss to counterbalance the weakened stealth performance.

The overall standoff boundary describes the distinguishability of signal photon counts from noise counts across the entire time interval. At the overall standoff boundary with $B = 100$ kbits, Willie's average signal photon rate $\lambda_s^{(W)}$ is $9 \times 10^3 \,\mathrm{s}^{-1}$, which is significantly less than the average noise rate $\lambda_n^{(W)} = 1 \times 10^5 \,\mathrm{s}^{-1}$. Moreover, the peak power standoff boundary in Fig. 3 assesses the distinguishability between signal and noise at the scale of a pulsed slot in the PPM symbol. Within such a slot, the average photon count is only 0.06, significantly less than the noise average of 0.2. These stark contrasts between signal and noise counts underscore that the probabilistic definitions of standoff boundaries are far more stringent than intuitive definitions, typically represented by the boundary where the signal count in a slot equals the noise count. As illustrated in Fig. 3, the signal-equals-noise boundary can lead to an overestimation of the covert performance of a transmission.

Practical UV communication systems commonly employ continuous lasers or LED arrays as light sources [31], [32], which operate at power levels P_{ON} significantly lower than
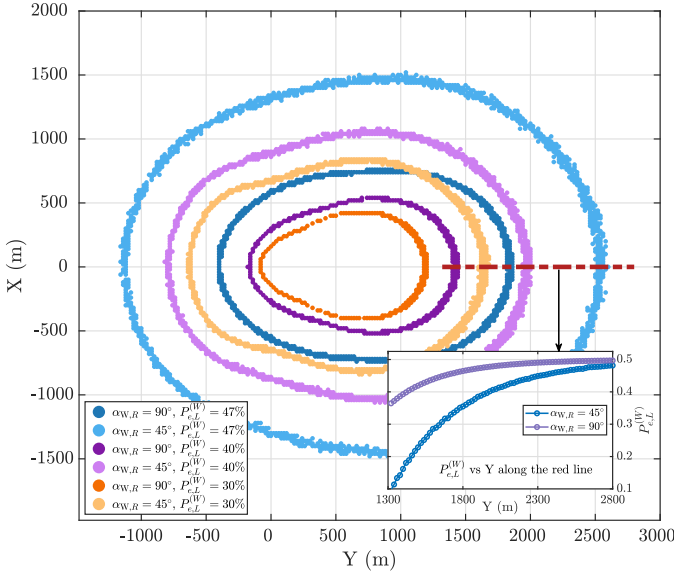
Fig. 4. Boundary patterns for various lower bounds of Willie's discrimination error probability at different elevation angles.

those of high-energy pulsed lasers [33]. When transmitting a substantial number of bits, the peak power standoff boundary tends to be encompassed within the overall standoff boundary, as shown in Fig. 3. In other words, successful covert communication under the peak power metric does not necessarily guarantee covert performance when the total photon-count criterion is applied. Thus, we consider the peak power metric weaker than the total photon counting metric unless high-energy pulsed lasers are employed as the UV communication source.

Figure 4 shows the overall standoff boundary when Willie incidentally aligns his receiver's azimuth towards Alice's location with an elevation angle of $45°$ and $90°$. This alignment increases the likelihood of Willie's FOV intersecting with Alice's emitted beam, facilitating a more effective scattered link for NLOS transmission and resulting in the reception of a greater number of photons. Enhanced photon reception amplifies the detectability of Alice's transmission and the discriminability between signal and noise, consequently expanding the overall standoff boundary. Moreover, different lower bounds of Willie's detection error probability are also shown in Fig. 4. As the distance between Willie and Alice increases, the number of photons received by Willie rapidly decreases, causing his lower bound detection error probability to approach 50%. Notably, within the most detectable forward transmission area of the Alice-to-Bob channel, even at a distance of $2000\,\mathrm{m}$, the lower bound of Willie's detection error probability remains above 40%, regardless of whether Willie is oriented towards Alice.

Figure 5 illustrates the impact of varying the transmitter's elevation angle on the communication coverage area of the Alice-to-Bob channel, as well as on the overall and peak power standoff boundaries of the Alice-to-Willie channel, where the lower bound of Willie's detection error probability is set at 40%. As the elevation angle decreases, both the standoff boundary and communication range within the depicted areas
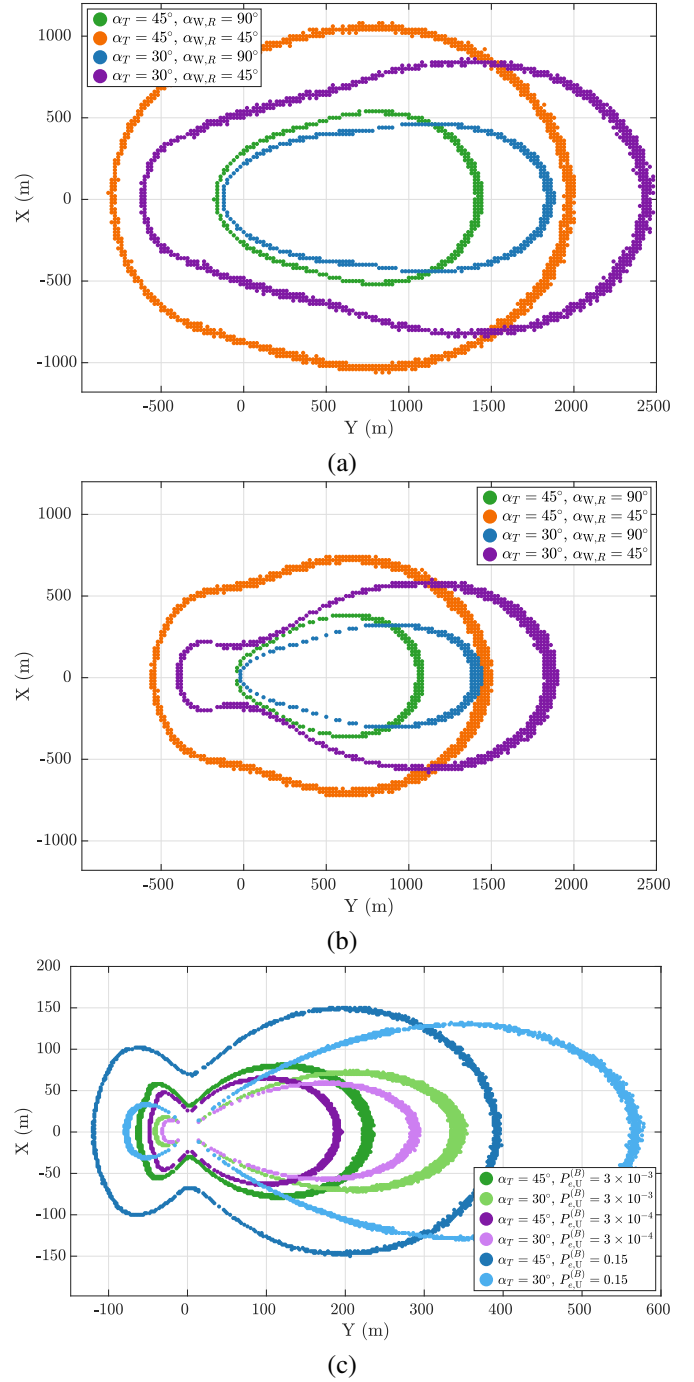

(a)

(b)

(c)

Fig. 5. Standoff and communication boundaries under various Alice's elevation angles: (a) overall standoff boundaries; (b) peak power standoff boundaries; (c) communication coverage.

become more elongated, exhibiting increased anisotropy. This anisotropy reflects a significant directional dependency in the spatial distribution of the received signals, underscoring the sensitivity of NLOS communication to angular adjustments of the transmitter. Furthermore, the communication coverage for different BER thresholds is shown in Fig. 5c. As the distance extends, the received signal photon counts decay rapidly, leading to a corresponding sharp rise in the BER. This characteristic effectively underscores the superior confidentiality offered by UV communications under PLS, another technique

for secure transmission beyond covert communication theory. The primary objective of PLS is to prevent eavesdroppers from decoding secure data by reducing the signal-to-noise ratio at the eavesdropper's receiver. Furthermore, PLS requires only that an eavesdropper fails to demodulate the signal, making its security standard significantly less stringent than that of covert communication, which necessitates that the transmission itself remains undetectable. As a result, the security distance in PLS is considerably shorter than the standoff distance in covert communication.

In general, a PPM-based UV communication system with a $200\,\mathrm{m}$ communication range corresponds to a maximal standoff distance of around $2000\,\mathrm{m}$. This standoff distance is obtained under optimal eavesdropping conditions. Specifically, the eavesdropper is assumed to deploy the same photon-level[2] receiver as the legitimate user, achieve perfect horizontal alignment with the transmitter, coincidentally synchronize the monitoring window to the transmission window, and possess comprehensive knowledge of the ambient UV noise level. These assumptions substantially enhance the eavesdropper's capability to detect UV transmission, making it more challenging for UV transmissions to remain stealthy. Even so, our results indicate that at $2000\,\mathrm{m}$ from Alice, the extremely high attenuation of UV signals prevents the eavesdropper from receiving enough UV signal power to determine the presence of a UV transmission reliably, underscoring the covert potential of UV communications. By comparison, a standard Bluetooth device designed for $10\,\mathrm{m}$ operation can be intercepted and eavesdropped from $1600\,\mathrm{m}$ away by an eavesdropper using a high-gain directional antenna [34], [35], indicating a detection range well beyond $1600\,\mathrm{m}$. This is because RF signals experience far less attenuation in free space compared to UV signals, enabling them to propagate over substantially greater distances. Consequently, a standoff distance of $2000\,\mathrm{m}$ for a $200\,\mathrm{m}$ UV NLOS link reflects a substantially stronger stealth capability than standard short-range RF systems.

This study excludes cooperative jamming, which is frequently used in RF covert communications to enhance transmission stealth [36], [37]. By artificially raising the eavesdropper's background noise level, the jamming signal makes it more likely that Willie fails to detect Alice's transmissions. Notably, in most RF scenarios, the presence of a jammer is typically assumed to be known to the eavesdropper. A similar idea can be applied in UV communications if a jammer is explicitly permitted. In that case, the cooperative jamming signal can elevate the noise level λ_n on Willie's side, thereby reducing the probability of detecting Alice's UV broadcast signals and increasing the probability of discrimination error in Theorem 1 and (6).

Nevertheless, one of the unique advantages of UV communications lies in short-range, NLOS links, particularly in outdoor environments. If the eavesdropper accurately knows the local background noise level, any additional energy introduced by a jammer would deviate from that noise profile,

likely alerting the eavesdropper to the presence of a UV transmitter. Practically speaking, jamming energy adds to UV signal level $\lambda_s^{(W)}$ rather than simply boosting λ_n in (6), which can undermine the natural stealth of UV signals. Given that our work focuses on UV communications operating under adverse conditions for secure transmission, we assume the eavesdropper is fully aware of the natural background noise. Conclusively, all our analysis focuses on evaluating how well UV signals—by virtue of their inherent attenuation characteristics—remain undetectable within that natural background noise. This natural covert performance analysis does not include cooperative jamming.

VI. CONCLUSION

In this study, we employed covert communication metrics to quantitatively analyze the security performance and standoff distances in UV NLOS communications. We introduced overall photon counting based and peak power based metrics, which together provide a comprehensive depiction of the security performance across different channel observation strategies used by eavesdroppers. Moreover, by integrating these proposed metrics with the updated UV omni-directional transmission model, we established, for the first time, standoff boundaries for UV NLOS transmission. The standoff boundaries quantitatively describe the confidentiality performance of the UV NLOS communication across varying distances. The results highlight the potential of this modeling and analytical approach to offer critical insights into the design and operational strategies of low-probability-of-detection NLOS UV communication systems. This work underscores the significant role of covert metrics in enhancing the security frameworks of optical wireless communications.

APPENDIX A
DERIVATION OF $f'(0)$ AND $f''(0)$ IN (18)

Based on $\mathcal{D}\left(\mathbb{P}_{0,W_j^{\mathrm{III}}}\|\mathbb{P}_{1,W_j^{\mathrm{III}}}\right) \triangleq f\left(\frac{1}{Q}\right)$ in (17), we can obtain the first derivative of $f\left(\frac{1}{Q}\right)$ at $\frac{1}{Q}=0$ as follows

$$
\begin{aligned}
f'(0) = & -\sum_{w_j^{\mathrm{III}}=0}^{\infty} p_{0,W_j^{\mathrm{III}}}\left(w_j^{\mathrm{III}}\right) \\
& \times \left(-1+e^{-\lambda_s^{(W)}T_s}\left(1+\frac{\lambda_s^{(W)}}{\lambda_n}\right)^{w_j^{\mathrm{III}}}\right) \\
= & \sum_{w_j^{\mathrm{III}}=0}^{\infty} \frac{(\lambda_n T_s)^{w_j^{\mathrm{III}}} e^{-\lambda_n T_s}}{w_j^{\mathrm{III}}!} \\
& -\sum_{w_j^{\mathrm{III}}=0}^{\infty} \frac{\left((\lambda_n+\lambda_s^{(W)})T_s\right)^{w_j^{\mathrm{III}}} e^{-(\lambda_n+\lambda_s^{(W)})T_s}}{w_j^{\mathrm{III}}!} \\
= & 0.
\end{aligned}
\tag{33}
$$

[2]In this work, we regard a single photon as the fundamental quantum of optical energy, serving as the minimal optical energy unit.

This article has been accepted for publication in IEEE Transactions on Wireless Communications. This is the author's version which has not been fully edited and content may change prior to final publication. Citation information: DOI 10.1109/TWC.2025.3564322

11

Then, the second derivative of $f\left(\frac{1}{Q}\right)$ at $\frac{1}{Q} = 0$ can be obtained as

$$
\begin{aligned}
f''(0) &= \sum_{w_j^{\mathrm{III}}=0}^{\infty} p_{0,W_j^{\mathrm{III}}}\left(w_j^{\mathrm{III}}\right) \\
&\quad \times \left(-1 + e^{-\lambda_s^{(W)}T_s}\left(1+\frac{\lambda_s^{(W)}}{\lambda_n}\right)^{w_j^{\mathrm{III}}}\right)^2 \\
&= -1 + \sum_{w_j^{\mathrm{III}}=0}^{\infty} \frac{(\lambda_n T_s)^{w_j^{\mathrm{III}}} e^{-\lambda_n T_s}}{w_j^{\mathrm{III}}!} \\
&\quad \times \left(1+\frac{\lambda_s^{(W)}}{\lambda_n}\right)^{2w_j^{\mathrm{III}}} e^{-2\lambda_s^{(W)}T_s} \\
&= -1 + \sum_{w_j^{\mathrm{III}}=0}^{\infty} \frac{\left(\left(\lambda_n + \frac{\left(\lambda_s^{(W)}\right)^2}{\lambda_n} + 2\lambda_s^{(W)}\right)T_s\right)^{w_j^{\mathrm{III}}}}{w_j^{\mathrm{III}}!} \\
&\quad \times e^{-\left(\lambda_n+\frac{\left(\lambda_s^{(W)}\right)^2}{\lambda_n}+2\lambda_s^{(W)}\right)T_s} e^{\frac{\left(\lambda_s^{(W)}\right)^2 T_s}{\lambda_n}} \\
&= e^{\frac{\left(\lambda_s^{(W)}\right)^2 T_s}{\lambda_n}} - 1 \\
&= \frac{\left(\lambda_s^{(W)}\right)^2 T_s}{\lambda_n} + \sum_{i=1}^{\infty} \frac{1}{i!}\left(\frac{\left(\lambda_s^{(W)}\right)^2 T_s}{\lambda_n}\right)^i .
\end{aligned}
\tag{34}
$$

APPENDIX B
DERIVATION OF $f_{\mathrm{L}}'(0)$, AND $f_{\mathrm{L}}''(0)$ IN (25)

Based on $\mathcal{D}\left(\mathbb{P}_{0,W_j^{\mathrm{III}}}\|\mathbb{P}_{1,W_{\mathrm{L},j}^{\mathrm{III}}}\right) \triangleq f_{\mathrm{L}}\left(\frac{1}{Q}\right)$ in (24), we can obtain the first derivative of $f_{\mathrm{L}}\left(\frac{1}{Q}\right)$ at $\frac{1}{Q}=0$ as follows

$$
\begin{aligned}
f_{\mathrm{L}}'(0) &= -\sum_{w_j^{\mathrm{III}}=0}^{\infty} p_{0,W_j^{\mathrm{III}}}\left(w_{\mathrm{L},j}^{\mathrm{III}}\right) \\
&\quad \times \left(-Q_d + \sum_{i=1}^{Q_d} e^{-\Lambda_{s,i}^{(W)}}\left(1+\frac{\Lambda_{s,i}^{(W)}}{\lambda_n T_s}\right)^{w_{\mathrm{L},j}^{\mathrm{III}}}\right) \\
&= \sum_{w_{\mathrm{L},j}^{\mathrm{III}}=0}^{\infty} p_{0,W_j^{\mathrm{III}}}\left(w_{\mathrm{L},j}^{\mathrm{III}}\right) \sum_{i=1}^{Q_d} e^{-\Lambda_{s,i}^{(W)}}\left(1+\frac{\Lambda_{s,i}^{(W)}}{\lambda_n T_s}\right)^{w_{\mathrm{L},j}^{\mathrm{III}}} \\
&\quad - Q_d \sum_{w_j^{\mathrm{III}}=0}^{\infty} p_{0,W_j^{\mathrm{III}}}\left(w_{\mathrm{L},j}^{\mathrm{III}}\right) \\
&= \sum_{i=1}^{Q_d} \sum_{w_{\mathrm{L},j}^{\mathrm{III}}=0}^{\infty} \frac{\left(\lambda_n T_s + \Lambda_s^{(W)}\right)^{w_j^{\mathrm{III}}} e^{-\left(\lambda_n T_s + \Lambda_s^{(W)}\right)}}{w_{\mathrm{L},j}^{\mathrm{III}}!} \\
&\quad - Q_d \sum_{w_j^{\mathrm{III}}=0}^{\infty} p_{0,W_j^{\mathrm{III}}}\left(w_{\mathrm{L},j}^{\mathrm{III}}\right) \\
&= 0.
\end{aligned}
\tag{35}
$$

Meanwhile, the second derivative of the function $f_{\mathrm{L}}\left(\frac{1}{Q}\right)$ can be calculated by

$$
\begin{aligned}
f_{\mathrm{L}}''(0) &= \sum_{w_{\mathrm{L},j}^{\mathrm{III}}=0}^{\infty} p_{0,W_j^{\mathrm{III}}}\left(w_{\mathrm{L},j}^{\mathrm{III}}\right) \\
&\quad \times \left(-Q_d + \sum_{i=1}^{Q_d} e^{-\Lambda_{s,i}^{(W)}}\left(1+\frac{\Lambda_{s,i}^{(W)}}{\lambda_n T_s}\right)^{w_{\mathrm{L},j}^{\mathrm{III}}}\right)^2 \\
&= -Q_d^2 + \sum_{w_{\mathrm{L},j}^{\mathrm{III}}=0}^{\infty} p_{0,W_j^{\mathrm{III}}}\left(w_{\mathrm{L},j}^{\mathrm{III}}\right) \\
&\quad \times \left(\sum_{i=1}^{Q_d} e^{-\Lambda_{s,i}^{(W)}}\left(1+\frac{\Lambda_{s,i}^{(W)}}{\lambda_n T_s}\right)^{w_{\mathrm{L},j}^{\mathrm{III}}}\right)^2 \\
&= -Q_d^2 + \sum_{w_{\mathrm{L},j}^{\mathrm{III}}=0}^{\infty} p_{0,W_j^{\mathrm{III}}}\left(w_{\mathrm{L},j}^{\mathrm{III}}\right)\left(\sum_{m=1}^{Q_d}\sum_{n=1}^{Q_d} e^{-\Lambda_{s,m}^{(W)}-\Lambda_{s,n}^{(W)}}\right. \\
&\quad \left. \times \left[\left(1+\frac{\Lambda_{s,m}^{(W)}}{\lambda_n T_s}\right)\left(1+\frac{\Lambda_{s,n}^{(W)}}{\lambda_n T_s}\right)\right]^{w_{\mathrm{L},j}^{\mathrm{III}}}\right) \\
&= -Q_d^2 + \sum_{m=1}^{Q_d}\sum_{n=1}^{Q_d} e^{\frac{\Lambda_{s,m}^{(W)}\Lambda_{s,n}^{(W)}}{\lambda_n T_s}} \\
&\quad \times \sum_{w_{\mathrm{L},j}^{\mathrm{III}}=0}^{\infty} \frac{\left(\lambda_n T_s + \frac{\Lambda_{s,m}^{(W)}\Lambda_{s,n}^{(W)}}{(\lambda_n T_s)^2} + \frac{\Lambda_{s,m}^{(W)}+\Lambda_{s,n}^{(W)}}{\lambda_n T_s}\right)^{w_j^{\mathrm{III}}}}{w_{\mathrm{L},j}^{\mathrm{III}}!} \\
&\quad \times e^{-\lambda_n T_s - \frac{\Lambda_{s,m}^{(W)}\Lambda_{s,n}^{(W)}}{(\lambda_n T_s)^2} - \frac{\Lambda_{s,m}^{(W)}+\Lambda_{s,n}^{(W)}}{\lambda_n T_s}} \\
&= \sum_{m=1}^{Q_d}\sum_{n=1}^{Q_d}\left(e^{\frac{\Lambda_{s,m}^{(W)}\Lambda_{s,n}^{(W)}}{\lambda_n T_s}} - 1\right) \\
&\approx \sum_{m=1}^{Q_d}\sum_{n=1}^{Q_d} \frac{\Lambda_{s,m}^{(W)}\Lambda_{s,n}^{(W)}}{\lambda_n T_s} \\
&= \frac{\left(\sum_{m=1}^{Q_d}\Lambda_{s,m}^{(W)}\right)^2}{\lambda_n T_s} = \frac{\left(\lambda_s^{(W)}\right)^2 T_s}{\lambda_n},
\end{aligned}
\tag{36}
$$

where the approximate equality sign holds true when $\frac{\Lambda_{s,m}^{(W)}\Lambda_{s,n}^{(W)}}{\lambda_n T_s}$ is small.

APPENDIX C
OMNI-DIRECTIONAL NLOS MONTE CARLO ALGORITHM

Algorithem 1 illustrates the algorithm structure employed for Monte-Carlo integration in UV NLOS omni-directional communication. The inputs (α_T, β_T), (α_R, β_R) are the geometrical configurations defined in Section V. (k_a, k_r, k_m) are the atmospheric parameters corresponding to absorption coefficient, Rayleigh scattering coefficient and Mie scattering coefficient, respectively. (γ, g, f) are the model parameters in the scattering phase function; $\{T_q\}, q = 1, 2\cdots, Q$, are time slots for calculating the channel impulse response. $\{A_{(i,j)}\}, i = 1, 2\cdots, I, j = 1, 2\cdots, J$, represents the positions of the square sub-areas for calculating the probability of

---

Algorithm 1 Omni-directional NLOS Model

Input: $(\alpha_T, \beta_T), (\alpha_R, \beta_R), S_r, (k_a, k_r, k_m), (\gamma, g, f), N_P, l,$
  $N_M, \{T_q, 1 \le q \le Q\}, \{A_{i,j}, 1 \le i \le I, 1 \le j \le J,\}$

Output: $[\boldsymbol{C}]_{(I,J,Q)}$

1: $\boldsymbol{C} \leftarrow 0, \forall i, j, q$
2: $k_s \leftarrow k_r + k_m$
3: $k_e \leftarrow k_a + k_s$
4: $c \leftarrow 2.997\,046 \times 10^8$
5: $\boldsymbol{\mu}_T = (\mu_{T,x}, \mu_{T,y}, \mu_{T,z})^T \leftarrow [0, \cos\alpha_T, \sin\alpha_T]^T$
6: **for** $k \leftarrow 1$ to N_P **do**
7:     $\boldsymbol{r} = (r_x, r_y, r_z)^T \leftarrow [0, 0, 0]^T$
8:     $d_{\mathrm{cur}} \leftarrow 0$
9:     $\theta_T \leftarrow \arccos\left(1 - \mathrm{rand}(1)(1 - \cos(\beta_T/2))\right)$
10:    $\phi_T \leftarrow 2\pi \cdot \mathrm{rand}(1)$
11:    $\boldsymbol{\mu} = (\mu_x, \mu_y, \mu_z)^T \leftarrow f_\mu(\boldsymbol{\mu}_T, \theta_T, \phi_T)$
12:    **for** $n \leftarrow 1$ to N_M **do**
13:       $d \leftarrow \log[1 - \mathrm{rand}(1)]/k_e$
14:       $\boldsymbol{r} \leftarrow \boldsymbol{r} + d \cdot \boldsymbol{\mu}$
15:       $d_{cur} \leftarrow d_{cur} + d$
16:       $\theta \leftarrow \pi \cdot \mathrm{rand}(1)$
17:       $\phi \leftarrow 2\pi \cdot \mathrm{rand}(1)$
18:       $O_n^* \leftarrow k_s/k_e \cdot \pi \cdot f_\Theta(\theta)$
19:       $\boldsymbol{\mu} \leftarrow f_\mu(\boldsymbol{\mu}, \theta, \phi)$
20:       **if** $\mu_z < 0$ **then**
21:         $\boldsymbol{r}_{n,R} = (r_{n,R,x}, r_{n,R,y}, r_{n,R,z})^T \leftarrow \boldsymbol{r} + \boldsymbol{\mu} \cdot |r_z/\mu_z|$
22:         $\boldsymbol{\mu}_R \leftarrow [r_{n,R,x}, r_{n,R,y}, \|\boldsymbol{r}_{n,R}\| \cdot \tan\alpha_R]^T$
23:         $\cos\phi_r \leftarrow \boldsymbol{\mu}_R \cdot \boldsymbol{r}/(\|\boldsymbol{r}\| \cdot \|\boldsymbol{\mu}_R\|)$
24:         **if** $\cos\phi_r \ge \cos(\beta_R/2)$ **then**
25:           $d_{\mathrm{total}} \leftarrow d_{cur} + |r_z/\mu_z|)$
26:           $\theta \leftarrow \beta_r/2 \cdot \mathrm{rand}(1)$
27:           $P_d \leftarrow \exp\left(-k_e \cdot |r_z/\mu_z|\right) \cdot \Pi_n O_n^*$
28:           Compute q s.t. $d_{\mathrm{total}}/c \in T_q$
29:           Compute (i, j) s.t. $\boldsymbol{\mu}_R \in A_{i,j}$
30:           $[\boldsymbol{C}]_{(i,j,q)} \leftarrow [\boldsymbol{C}]_{(i,j,q)} + P_d$
31:         **end if**
32:       **end if**
33:     **end for**
34:   **end for**
35: $\boldsymbol{C} \leftarrow \boldsymbol{C} \cdot S_r/(N_P l^2 \sin\alpha_R)$

---

photon reception at different positions. l is the side length of all the square sub-areas. S_r is the receiving aperture area. N_P and N_M denote the number of simulation photons and the highest scattering order, respectively. The output $[\boldsymbol{C}]_{(I,J,Q)}$ is a three-dimensional matrix describing the channel impulse response over all the sub-areas. By summing across the third dimension of the matrix $\boldsymbol{C}$, we obtain a two-dimensional matrix representing the channel gain at different positions across the entire area.

In **Algorithem** 1, lines 9-11 randomly generate the directions of photon emissions $\boldsymbol{\mu}_0$, where f_μ compute the new direction cosine $\boldsymbol{\mu} = (\mu_x, \mu_y, \mu_z)^T$ from the transmitter's direction cosine $\boldsymbol{\mu_T}$ and the emission zenith angle θ_T and emission azimuth angle ϕ_T. Line 13 samples the propagation distance based on the Beer-Lambert law, in which the PDF for the propagating distance is $f_D(d_n) = k_e e^{-k_e d_n}, 0 \le d_n \le \infty$

with $k_e = k_s + k_a$ representing the extinction coefficient of the transmission medium, comprising both scattering (k_s) and absorption (k_a) coefficients. Line 14 computes the position of the scattering event; lines 16-17 sample the scattering zenith angle and scattering azimuth angle from the uniform distribution; The corresponding objective function is computed in line 18 using the PDF of scattering zenith angle $f_\Theta(\theta_n)$ as [10]

$$f_{\Theta_n}(\theta_n) = \frac{k_r}{k_s} f_{\Theta_n}^{Ray}(\theta_n) + \frac{k_m}{k_s} f_{\Theta_n}^{Mie}(\theta_n), \quad 0 \le \theta_n \le \pi \quad (37)$$

where k_r and k_m are the scattering coefficients for Rayleigh scattering and Mie scattering, respectively. The Rayleigh scattering component is modeled as

$$f_{\Theta_n}^{Ray}(\theta_n) = \frac{3[1 + 3\gamma + (1 - \gamma)\cos^2\theta_n]}{8(1 + 2\gamma)}\sin\theta_n, \quad (38)$$

and the Mie scattering component is given by

$$f_{\Theta_n}^{Mie}(\theta_n) = \frac{1 - g^2}{2}\left[\frac{1}{(1 + g^2 - 2g\cos\theta_n)^{\frac{3}{2}}} + f\frac{0.5(3\cos^2\theta_n - 1)}{(1 + g^2)^{\frac{3}{2}}}\right]\sin\theta_n \quad (39)$$

where the constants γ, g and f are empirical constants specific to the scattering model.

Line 20 determines if the direction after scattering is towards the ground, while line 21 calculates the position where the photon reaches the ground. If the photon is within the FOV of the receiver at this location (as checked in line 24), lines 25-30 update the probability of photon reception and the photon's arrival time, where line 29 calculates the index (i, j) of the activated sub-area based on photon's landing position $\boldsymbol{r}_{n,R}$ and the side length l of the square sub-areas; line 35 computes the output three-dimensional matrix $[\boldsymbol{C}]_{(I,J,Q)}$. The matrix $\boldsymbol{C}$ comprehensively describes both the path loss and the channel impulse response for all the sub-areas in the simulated region. Specifically, the channel gain can be represented by a $I \times J$ matrix, where each element corresponds to the channel gain of the respective area, derived by summing over the third dimension of matrix $\boldsymbol{C}$. Additionally, the $1 \times 1 \times Q$ one-dimensional array $\boldsymbol{C}(i, j, :)$ describes the channel impulse response for the pixel (i, j).

TABLE II
Simulation Parameters in Omni-directional Model

Parameters	Value
S_r	$1.77 \times 10^{-4}\,\mathrm{m}^2$
γ	0.017
g	0.5
f	0.72
k_a	$0.802 \times 10^{-3}\,\mathrm{m}^{-1}$
k_r	$0.266 \times 10^{-3}\,\mathrm{m}^{-1}$
k_m	$0.284 \times 10^{-3}\,\mathrm{m}^{-1}$
τ	$10\,\mathrm{ns}$
l	$5\,\mathrm{m}$
N_M	3

The required simulation parameters are listed in Table II. All the simulations are conducted using Matlab R2022a on a desktop computer with a $3.2\,\mathrm{GHz}$ CPU and $128\,\mathrm{GB}$ RAM.

This article has been accepted for publication in IEEE Transactions on Wireless Communications. This is the author's version which has not been fully edited and content may change prior to final publication. Citation information: DOI 10.1109/TWC.2025.3564322

13

For these simulations, we used a total of 1×10^{10} simulation photons and a simulation time of $40\,000\,\text{s}$.

References

[1] M. Uysal, C. Capsoni, A. Boucouvalas, and E. Udvary, *Optical Wireless Communications – An Emerging Technology*. Springer, 2017.

[2] A. Vavoulas, H. G. Sandalidis, N. D. Chatzidiamantis, Z. Xu, and G. K. Karagiannidis, "A survey on ultraviolet c-band (UV-C) communications," *IEEE Commun. Surv. Tutor.*, vol. 21, no. 3, pp. 2111–2133, 3rd Quart. 2019.

[3] Z. Xu and B. M. Sadler, "Ultraviolet communications: Potential and state-of-the-art," *IEEE Communications Magazine*, vol. 46, no. 5, pp. 67–73, 2008.

[4] R. Yuan, S. Wang, G. Liu, and M. Peng, "Non-line-of-sight ultraviolet positioning using linearly-arrayed photon-counting receivers," *IEEE J.Sel. Areas Commun.*, vol. 42, no. 9, pp. 2535–2549, Sep. 2024.

[5] G. A. Shaw, M. L. Nischan, M. A. Iyengar, S. Kaushik, and M. K. Griffin, "NLOS UV communication for distributed sensor systems," in *Integrated Command Environments*, P. Hamburger, Ed., vol. 4126, International Society for Optics and Photonics. SPIE, Nov. 2000, pp. 83 – 96.

[6] D. M. Reilly, D. T. Moriarty, and J. A. Maynard, "Unique properties of solar blind ultraviolet communication systems for unattended ground sensor networks," in *Unmanned/Unattended Sensors and Sensor Networks*, E. M. Carapezza, Ed., vol. 5611, International Society for Optics and Photonics. SPIE, Nov. 2004, pp. 244 – 254.

[7] M. J. Weisman, F. T. Dagefu, T. J. Moore, C. H. Arslan, and R. J. Drost, "Analysis of the low-probability-of-detection characteristics of ultraviolet communications," *Opt. Express*, vol. 28, no. 16, pp. 23 640–23 651, Aug. 2020.

[8] H. Ding, G. Chen, A. K. Majumdar, B. M. Sadler, and Z. Xu, "Modeling of non-line-of-sight ultraviolet scattering channels for communication," *IEEE J. Sel. Areas Commun.*, vol. 27, no. 9, pp. 1535–1544, 2009.

[9] R. J. Drost, T. J. Moore, and B. M. Sadler, "UV communications channel modeling incorporating multiple scattering interactions," *J. Opt. Soc. Am. A*, vol. 28, no. 4, pp. 686–695, Apr. 2011.

[10] R. Yuan, J. Ma, P. Su, Y. Dong, and J. Cheng, "Monte-carlo integration models for multiple scattering based optical wireless communication," *IEEE Trans. Commun.*, vol. 68, no. 1, pp. 334–348, Jan. 2020.

[11] M. R. Luettgen, D. M. Reilly, and J. H. Shapiro, "Non-line-of-sight single-scatter propagation model," *J. Opt. Soc. Am. A*, vol. 8, no. 12, pp. 1964–1972, Dec. 1991.

[12] Z. Xu, H. Ding, B. M. Sadler, and G. Chen, "Analytical performance study of solar blind non-line-of-sight ultraviolet short-range communication links," *Opt. Lett.*, vol. 33, no. 16, pp. 1860–1862, Aug 2008.

[13] T. Wu, J. Ma, R. Yuan, P. Su, and J. Cheng, "Single-scatter model for short-range ultraviolet communication in a narrow beam case," *IEEE Photonics Technology Letters*, vol. 31, no. 3, pp. 265–268, 2019.

[14] R. Yuan and J. Ma, "Review of ultraviolet non-line-of-sight communication," *China Communications*, vol. 13, no. 6, pp. 63–75, 2016.

[15] Z. Shen, J. Ma, T. Shan, and T. Wu, "Modeling of ultraviolet scattering propagation and its applicability analysis," *Opt. Lett.*, vol. 44, no. 20, pp. 4953–4956, Oct 2019.

[16] T. Shan, J. Ma, T. Wu, Z. Shen, and P. Su, "Modeling of ultraviolet omni-directional multiple scattering channel based on Monte Carlo method," *Opt. Lett.*, vol. 45, no. 20, pp. 5724–5727, Oct. 2020.

[17] T. Shan, R. Yuan, N. He, and J. Cheng, "Non-line-of-sight ultraviolet transmission coverage in non-precipitating, foggy, and rainy weather," *Opt. Express*, vol. 31, no. 23, pp. 37 703–37 721, Nov. 2023.

[18] X. Chen, J. An, Z. Xiong, C. Xing, N. Zhao, F. R. Yu, and A. Nallanathan, "Covert communications: A comprehensive survey," *IEEE Commun. Surv. Tutor.*, vol. 25, no. 2, pp. 1173–1198, 2nd Quart. 2023.

[19] D. Zou, C. Gong, and Z. Xu, "Secrecy rate of MISO optical wireless scattering communications," *IEEE Trans. Commun.*, vol. 66, no. 1, pp. 225–238, Jan. 2018.

[20] B. A. Bash, D. Goeckel, and D. Towsley, "Limits of reliable communication with low probability of detection on AWGN channels," *IEEE J. Sel. Areas Commun.*, vol. 31, no. 9, pp. 1921–1930, Sep. 2013.

[21] B. A. Bash, A. H. Gheorghe, M. Patel, J. L. Habif, D. Goeckel, D. Towsley, and S. Guha, "Quantum-secure covert communication on bosonic channels," *Nat. Commun.*, vol. 6, no. 1, p. 8626, Oct. 2015.

[22] L. Wang, "Covert communication over the Poisson channel," *IEEE J. Sel. Areas Inf. Theory*, vol. 2, no. 1, pp. 23–31, Mar. 2021.

[23] Y. Yang, Y. Ren, W. Liu, C. Gong, N. Huang, and Z. Xu, "Spread spectrum for covert communication in ultra-violet communication system," *Opt. Express*, vol. 32, no. 15, pp. 25 981–25 994, July 2024.

[24] Z. Wang, R. Yuan, and M. Peng, "Non-line-of-sight full-duplex ultraviolet communications under self-interference," *IEEE Trans. Wireless Commun.*, vol. 22, no. 11, pp. 7775–7788, Nov. 2023.

[25] Z. Wang, R. Yuan, J. Cheng, and M. Peng, "Joint optimization of full-duplex relay placement and transmit power for multihop ultraviolet communications," *IEEE Internet Things J.*, vol. 11, no. 7, pp. 11 960–11 973, Apr. 2024.

[26] G. Chen, F. Abou-Galala, Z. Xu, and B. M. Sadler, "Experimental evaluation of led-based solar blind nlos communication links," *Opt. Express*, vol. 16, no. 19, pp. 15 059–15 068, Sep. 2008.

[27] Z. Wang, R. Yuan, and M. Peng, "Inter-symbol interferences deteriorated ultraviolet communications using photon-counting receivers," *IEEE Trans. Wireless Commun.*, vol. 23, no. 5, pp. 4097–4113, May 2024.

[28] R. M. Gagliardi and S. Karp, *Optical Communications*. New York: John Wiley & Sons, 1976.

[29] S. Yu, C. Gong, and Z. Xu, "Design and optimization of sandwich-type synchronization sequence for optical wireless communication with a photon-counting receiver," *IEEE Internet Things J.*, vol. 11, no. 9, pp. 15 880–15 893, May 2024.

[30] T. Shan and J. Cheng, "Coverage estimation for secure ultraviolet communication," in *MILCOM 2022 - 2022 IEEE Military Communications Conference (MILCOM)*, 2022, pp. 817–821.

[31] G. Wang, K. Wang, C. Gong, D. Zou, Z. Jiang, and Z. Xu, "A 1Mbps real-time NLOS UV scattering communication system with receiver diversity over 1km," *IEEE Photonics J.*, vol. 10, no. 2, pp. 1–13, Apr. 2018.

[32] G. Chen, Z. Xu, H. Ding, and B. M. Sadler, "Path loss modeling and performance trade-off study for short-range non-line-of-sight ultraviolet communications," *Opt. Express*, vol. 17, no. 5, pp. 3929–3940, Mar. 2009.

[33] G. Chen, Z. Xu, and B. M. Sadler, "Experimental demonstration of ultraviolet pulse broadening in short-range non-line-of-sight communication channels," *Opt. Express*, vol. 18, no. 10, pp. 10 500–10 509, May 2010.

[34] K. Haataja and P. Toivanen, "Two practical man-in-the-middle attacks on bluetooth secure simple pairing and countermeasures," *IEEE Trans. Wireless Commun.*, vol. 9, no. 1, pp. 384–392, Jan. 2010.

[35] D. Singelee and B. Preneel, "Location verification using secure distance bounding protocols," in *IEEE International Conference on Mobile Adhoc and Sensor Systems Conference, 2005.*, Nov. 2005, pp. 7 pp.–840.

[36] K.-W. Huang, H. Deng, and H.-M. Wang, "Jamming aided covert communication with multiple receivers," *IEEE Trans. Wireless Commun.*, vol. 20, no. 7, pp. 4480–4494, Jul. 2021.

[37] X. Chen, F. Gao, M. Qiu, J. Zhang, F. Shu, and S. Yan, "Achieving covert communication with a probabilistic jamming strategy," *IEEE Trans. Inf. Forensics Security*, vol. 19, pp. 5561–5574, May 2024.